Search for neutrino oscillations at a fission reactor

H. Kwon,* F. Boehm, A. A. Hahn,* H. E. Henrikson, and J.-L. Vuilleumier*
California Institute of Technology, Pasadena, California 91125

J.-F. Cavaignac, D. H. Koang, and B. Vignon
Institut des Sciences Nucleáires de Grenoble, IN2P3, 38026 Grenoble Cedex, France

F. v. Feilitzsch* and R. L. Mössbauer
Physik-Department, Technische Universität München, 8046, Garching, Federal Republic of Germany

(Received 7 April 1981)

The energy spectrum of neutrinos from a fission reactor was studied with the aim of gaining information on neutrino oscillations. The well-shielded detector was set up at a fixed position of 8.76 m from the pointlike core of the Laue-Langevin reactor in an antineutrino flux of 9.8×10^{11} cm^{-2} s^{-1}. The target protons in the reaction $\bar{\nu}_e p \rightarrow e^+ n$ were provided by liquid-scintillator counters (total volume of 377 l) which also served as positron detectors. The product neutrons moderated in the scintillator were detected by ^{3}He wire chambers. A coincidence signature was required between the prompt positron and the delayed neutron events. The positron energy resolution was 18% full width at half maximum at 0.91 MeV. The signal-to-background ratio was better than 1:1 between 2 and 6 MeV positron energy. At a counting rate of 1.58 counts per hour, 4890 ± 180 neutrino-induced events were detected. The shape of the measured positron spectrum was analyzed in terms of the parameters Δ^2 and $\sin^2 2\theta$ for two-neutrino oscillations. The experimental data are consistent with no oscillations. An upper limit of 0.15 eV^2 (90% C.L.) for the mass-squared differences Δ^2 of the neutrinos was obtained, assuming maximum mixing of the two-neutrino states. The ratio of the measured to the expected integral yield of positrons assuming no oscillations was determined to be $\int Y_{\rm exp}/\int Y_{\rm th} = 0.955\pm0.035$ (statistical) ± 0.110 (systematic).

I. INTRODUCTION

Among the most fascinating challenges today is the quest for the fundamental properties of neutrinos. The idea of neutrino mixing was first considered by Pontecorvo[1] for the ν-$\bar{\nu}$ system, in analogy to the K^0 system, and by Nakagawa *et al.*, and others,[2] for the ν_e-ν_μ system. The idea was that physical neutrinos are not pure states in a quantum-mechanical sense, but superpositions of mass eigenstates. Accordingly, the physical neutrinos oscillate in and out of their initial states, provided the mass differences of the pure states and the mixing amplitudes between them are nonvanishing. Gribov and Pontecorvo[3] suggested that the observed low flux of solar neutrinos[4] may be due to neutrino oscillations. Extended reviews on neutrino oscillations up to 1978 are contained in the articles by Fritzsch[5] and by Bilenky and Pontecorvo.[6]

Recently (while this experiment was in progress) neutrino oscillations have been discussed extensively[7] as being expected on theoretical grounds, creating new interest in the search for oscillations.

After the success of the SU(2) × U(1) Weinberg-Salam model[8] of the electroweak interaction, several more general models attempting to unify the strong and electroweak interactions have been proposed. According to some of these models (based on gauge symmetries), neutrinos are massive and could oscillate. Oscillations of the type $\nu_e \rightarrow \nu_\mu$ or $\nu_e \rightarrow \nu_\tau$ (flavor oscillations), or $\nu_e \rightarrow \bar{\nu}_{eL}$ (particle-antiparticle oscillations) might be expected. The symbol $\bar{\nu}_{eL}$ designates a left-handed electron antineutrino.

The present experimental limits on the masses of ν_e, ν_μ, and ν_τ are 35 eV,[9] 570 keV,[10] and 250 MeV,[11] respectively, which leaves ample room for the magnitude of various parameters describing neutrino oscillations. A recent experiment by Lyubimov *et al.*[12] suggests a finite mass of the electron neutrino in the range between 14 and 46 eV. However, this result is preliminary, awaiting confirmation.

Neutrinos also play an important role in the description of the early stage of the Universe. Cosmological theories set limits on the neutrino masses[13] and the number of neutrino types.[14] The commonly accepted cosmological limit on the sum of the masses of neutrinos is 40 eV.[15] But the cosmological arguments should only be used as a guide.

The neutrino oscillation is also connected with the fundamental question of lepton-number conservation. The mechanisms of $\mu \rightarrow e\gamma$ and double-β decay are closely related to neutrino oscillations. Consequently, in some models (which do not have heavy leptons), a limit on neutrino oscillations can impose more stringent limits on $\mu \rightarrow e\gamma$ and double-β decay than the current experiments are able to provide.

Several recent high-energy experiments have set limits for neutrino oscillations. However, these limits[16] are not very restrictive, nor do they pertain to all the possible oscillation chan-

nels. It is the purpose of this experiment to provide an answer, with better sensitivity, to the question: Are there oscillations of electron antineutrinos $\bar{\nu}_e$ produced in a fission reactor?

Recently, Reines *et al.*[17] have claimed evidence for $\bar{\nu}_e$ oscillations. Clearly, an independent confirmation of this observation is most important.

Phenomenological model for oscillations

A brief description of neutrino oscillations and the formalism which is relevant for the analysis of the experiment are presented below.

Neutrino oscillations of the weak-interaction eigenstates $(\nu_e, \nu_\alpha, \ldots)$ may occur if these "physical" neutrinos are superpositions of the mass eigenstates $(\nu_1, \nu_2, \ldots)$. If we confine our discussion to the case of a two-neutrino system (which might well approximate the general case), the superposition can be written as

$$\begin{pmatrix} \nu_e \\ \nu_\alpha \end{pmatrix} = \begin{pmatrix} \cos\theta & \sin\theta \\ -\sin\theta & \cos\theta \end{pmatrix} \begin{pmatrix} \nu_1 \\ \nu_2 \end{pmatrix},$$

where θ is a mixing parameter. This description[5,6,18] allows for flavor oscillations ($\nu_\alpha = \nu_\mu, \nu_\tau, \ldots$) as well as for particle-antiparticle oscillations ($\nu_\alpha = \bar{\nu}_{eL}, \ldots$). The time development of the system is given by

$$|\nu_e(t)|^2 = |\nu_e(0)|^2 \{1 - \tfrac{1}{2}\sin^2 2\theta [1 - \cos(E_2 - E_1)t]\},$$

where E_i is the energy of neutrino ν_i. For momenta $p \gg m_i$ (m_i being the mass), $E_2 - E_1 \approx (m_2^2 - m_1^2)/2p$.

The oscillation length λ (in meters) is related to the neutrino energy E_ν (in MeV) and the mass-squared difference $\Delta^2 = |m_2^2 - m_1^2|$ (in eV^2) by $\lambda = 2.48\, E_\nu/\Delta^2$.

The oscillations are thus characterized by the parameters Δ^2 and $\sin^2 2\theta$. The counting rate Y in a $\bar{\nu}$ detector at a distance d from an antineutrino source, such as the reactor core, is (using the same units) given by

$$Y(E_{\bar{\nu}}, \Delta^2 d, \theta) \sim \frac{\epsilon}{4\pi d^2} N(E_{\bar{\nu}}) \sigma(E_{\bar{\nu}}) P(E_{\bar{\nu}}, \Delta^2 d, \theta), \quad (1)$$

where

$$P(E_{\bar{\nu}}, \Delta^2 d, \theta) = 1 - \tfrac{1}{2}\sin^2 2\theta [1 - \cos(2.53\, \Delta^2 d/E_{\bar{\nu}})]. \quad (2)$$

$N(E_{\bar{\nu}})$ is the reactor-produced $\bar{\nu}$ spectrum and ϵ is the detection efficiency. The cross section $\sigma(E_{\bar{\nu}})$ (with $E_{\bar{\nu}}$ in MeV) of the detector reaction is discussed below.

The manifestations of the oscillations depend on the energy of the neutrino and the distance between source and detector. To detect neutrino oscillations, one has to measure the neutrino flux as a function of the energy, or the distance, or both. The present measurement was carried out as a function of energy, with good energy resolution, while the distance variation, for practical reasons, had to be postponed for a subsequent experiment.

At present the limits for Δ^2 in the channels $\nu_\mu \to \nu_e$ and $\bar{\nu}_\mu \to \bar{\nu}_e$ are 0.7 eV^2,[19] assuming full mixing. Limits for other channels are reviewed in Ref. 16.

II. EXPERIMENTAL METHOD

In this section the antineutrino source, the antineutrino detection reaction, the experimental setup, the data acquisition, and data reduction are discussed. The measurement of the detector efficiency is also presented.

Neutrino source and neutrino spectrum

The inverse β decay of the neutron, $\bar{\nu}_e + p \to e^+ + n$, which has the most favorable cross section, is used as the detection reaction.[20] The cross section is given by

$$\sigma(E_{\bar{\nu}}) = (9.13 \pm 0.11)(E_{\bar{\nu}} - 1.293) \times [(E_{\bar{\nu}} - 1.293)^2 - (0.511)^2]^{1/2} \times 10^{-44}\ \text{cm}^2$$

($E_{\bar{\nu}}$ is the neutrino kinetic energy in MeV). The error in the cross section stems from the uncertainty of the neutron lifetime,[21] $\tau = (926 \pm 11)$ s.

From energy-momentum conservation, the positron carries away most of the energy of the incoming neutrino. The neutron energy is around 20 keV. Therefore, the energy of the positron is simply related to the energy of the neutrino by $E_{e^+} = E_\nu - E_0$. The reaction threshold E_0 is given by $E_0 = (m_n - m_p) + m_e = 1.80$ MeV.

As a result, the positron energy spectrum conveys the information of the neutrino spectrum. A deviation of the measured positron spectrum from that expected without oscillations would indicate the presence of oscillations. The expected positron spectrum is the neutrino spectrum folded with the cross section and the detector efficiencies.

The experiment was carried out at the high-flux reactor of the Institut Laue-Langevin (ILL), Grenoble, France. The reactor has 57 MW thermal power (which remains constant to better than 1%). The fuel element of the reactor consists of 8.5 kg of 93% enriched ^{235}U in the form of UAl_3. This almost pure ^{235}U core has the advantage of lending itself to a well defined prediction of the electron-antineutrino spectrum. Fission energy release and neutrino production are time-dependent. For example, for each fission of ^{235}U, after

a 30-day period, 5.3 electron antineutrinos are emitted[22] as a result of β decays of the fission fragments. For the mean energy released per fission for one measuring period (40 days) (not including the antineutrino energy) we have taken 199 ± 2 MeV.[23] Thus the ILL reactor constitutes a source strength of 9.5×10^{18} electron antineutrinos per second.

The reactor core is a cylinder, 40 cm in diameter and 80 cm in height. This small "pointlike" core makes the ILL reactor ideal for studying short oscillation lengths for which the effects would be averaged out in measurements at a power reactor.

The operating cycle of the reactor consists of a 40-day reactor-on period followed by a 10-day reactor-off period. The reactor-off periods were used to measure the background.

The detector was designed with emphasis on good positron-energy resolution, low background, and high detection efficiency. The effect of oscillations would be washed out with poor energy resolution. A sensitivity to the parameter Δ^2 between 0.1 and 5 eV^2 should be achievable under these conditions.

The most appropriate and accurate method for obtaining the expected antineutrino spectrum emitted from the reactor core is a measurement of the electron spectrum accompanying ^{235}U fission. Such a measurement has recently been conducted[24] at ILL using an on-line magnetic β spectrometer. The accuracy of the relative shape measurement is 2% to which a normalization error of 5% has to be added. The uncertainty attributed to the neutrino spectrum, including a 4% conversion error, is 6.5%. In the following analysis we have adopted this ILL spectrum and shall refer to it as "expected neutrino spectrum for no oscillations".

A recent electron-spectrum measurement at ORNL (Ref. 25) tends to agree with the ILL results[24] although this experiment was not taken on-line and thus is less sensitive to short-lived fission fragments.

There are several calculations of the reactor antineutrino spectrum, notably those by Davis *et al.*[22] and by Avignone and Greenwood.[26] The uncertainty in the spectrum of Davis *et al.*[22] is estimated to be from 10% at 2 MeV to 30% at 8 MeV. The Davis *et al.* spectrum is found to be in good agreement with the ILL spectrum. In contrast, the spectrum of Ref. 26 is systematically 30% higher than the ILL results.

The antineutrinos emerging from the β decays of the surrounding material activated by the neutrons have low energies. In the case of the ILL reactor, the core contains aluminum which can emit antineutrinos with a maximum energy of 2.8 MeV. Since only events with $E_{e^+} > 1$ MeV (i.e., $E_{\bar{\nu}} > 2.8$ MeV) are accepted in this experiment, antineutrinos below 2.8 MeV are of no importance. About 16% of the fission-product antineutrinos have energies greater than 2.8 MeV.

Detection reaction

The detector is set up at an effective distance of 8.76 m (antineutrino flux of 9.8×10^{11} cm^{-2} s^{-1}) from the reactor core in the basement of the reactor building. The detector is a multilayer sandwich of five liquid-scintillator planes and four ^3He-wire-counter planes as shown in Fig. 1.

A schematic representation of the detection reaction is shown in Fig. 2. The antineutrino interacts with a proton of the liquid scintillator in the target cell, making a positron and a neutron. The positron slows down by ionization in the liquid scintillator producing a prompt light pulse proportional to the energy of the positron. Upon stopping, the positron annihilates into two 0.511-MeV γ rays. Most of the annihilation γ rays escape from the target cell, since their mean absorption length is 14 cm in the liquid scintillator. This effect was taken into account in the analysis. A hardware threshold was set at about 0.85 MeV.

The neutron (of a few keV) does not make a pulse in the liquid scintillator. Instead, it is thermalized in the target cell within a few μs and diffuses into the ^3He counter with a mean diffusion time of about 150 μs. The neutron is captured in a ^3He counter via the reaction $n + {}^3He \rightarrow p + {}^3H + 765$ keV. ^3He is chosen because it has a large neutron capture cross section

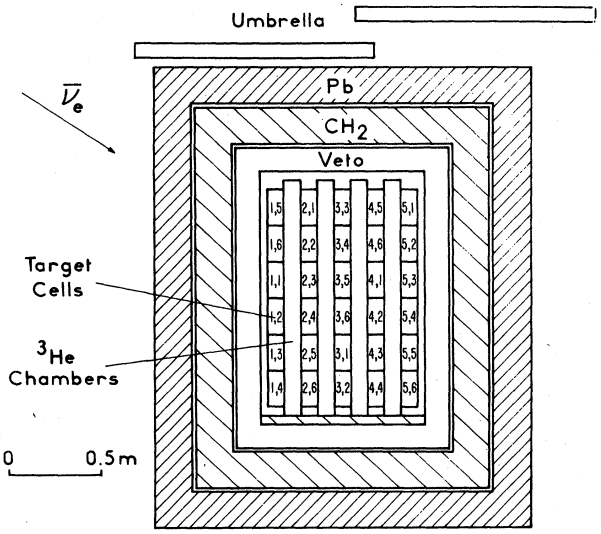

FIG. 1. Experimental arrangement of the detector system and shielding.

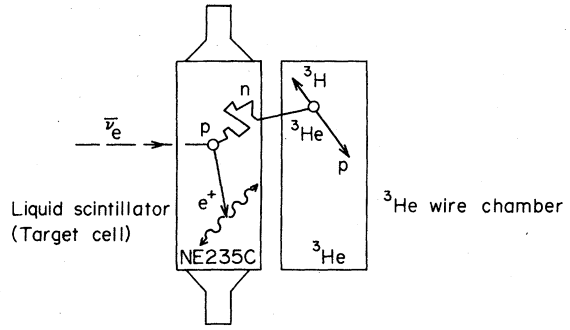

FIG. 2. Schematic representation of the $\bar{\nu}p \rightarrow e^+n$ reaction process in an element of the detector system.

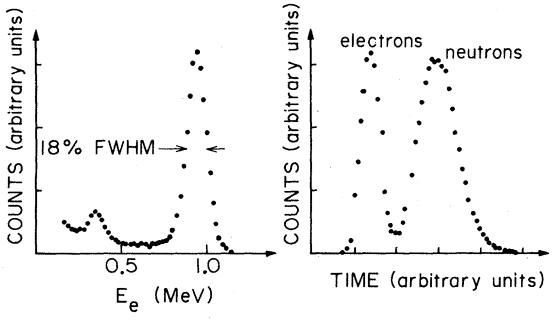

FIG. 3. Performances of the target cell. Left figure: energy spectrum of a ^{65}Zn source. Right figure: PSD spectrum for 1-MeV electron equivalent energy.

(5500 b for a thermal neutron) and because it is insensitive to γ rays due to the small number of electrons in the ^{3}He. Both the p and ^{3}H are detected by the ^{3}He wire counter which operates in the proportional region (multiplication factor about 10).

A delayed coincidence between target cell and ^{3}He counter pulses is the signature of a good event.

Background considerations

The background which gives rise to false events is divided into two categories: reactor-associated and reactor-independent. Each is subdivided into an accidental component and a time-correlated component, within the delayed-coincidence time window.

The reactor-associated background is due to neutrons and secondary capture γ rays of energies up to 10 MeV from the reactor core and was eliminated in this experiment by means of massive shielding.

The reactor-independent background is measured during the reactor-off periods. Care is taken to minimize the natural radioactivity in the detector in order to reduce the accidental coincidence rate. The more serious background comes from neutrons created in cosmic-ray-induced events. Fast and slow neutrons are created by the nucleonic and muonic components of cosmic rays. The nucleonic component is mostly eliminated by the concrete shielding above the detector. Direct muon hits are efficiently vetoed by the anticoincidence system, but neutrons from muons interacting in the surroundings of the detector are only partially rejected.

A particularly dangerous background component arises from time-correlated events due to single fast neutrons. A fast neutron can produce a recoil proton pulse in the target cell. The neutron subsequently thermalizes in the target cell and is captured in a ^{3}He counter, simulating an antineutrino event. To suppress this background, a pulse-shape-discrimination (PSD) technique[27] is used for the target-cell events.

Detector system: Target cells

The 30 target cells are arranged in five vertical planes of six cells in each plane. Each target cell has an outside dimension of 9 cm$\times$20 cm$\times$88 cm, and is made out of 6 mm lucite. The width of the cell was chosen to be thick enough for neutron thermalization, yet sufficiently thin to prevent excessive neutron absorption by the protons.

As a scintillant, a mineral-oil-based proton-rich liquid scintillator NE235C, developed by Nuclear Enterprises,[28] is used. The total volume of the scintillator is 377 l, corresponding to 2.39 $\times 10^{28}$ protons. (This scintillator is a modified version of NE235H with added pulse-shape properties.) NE235C has an H/C ratio of 1.71 $\pm$0.015 and a density of 0.861 g/cm^3. Its light output is 61.5% that of anthracene and the light transmission length is better than 2 m.

Each target cell is viewed at both ends by two optically coupled 7.5-cm Amperex XP2312 photomultiplier tubes. The XP2312 tube is a high-gain, fast-timing, low-dark-current tube. Total internal reflection at the air-lucite interface of the target-cell walls provides the light collection. To regain light not returned by total reflection, the cells are wrapped with alumininized reflectors. The end surfaces are covered by diffuse reflectors with an air gap for maximum light output.[29]

The target-cell energy resolution is 18% full width at half maximum (FWHM) at 0.91 MeV (Fig. 3). Variations in energy response throughout the volume of the cell are less than 5%. This result was obtained with forward-scattered Compton electrons from a single-line ^{65}Zn γ-ray source, the back-scattered γ rays being detected with a NaI detector in coincidence with the target cell.

For the absolute energy calibration the same method was used, this time based on the 4.439-

MeV γ rays in $^{12}C^*$ from an Am-Be source, and the Compton edge of the 2.226-MeV γ ray from neutron capture on the proton. The energy calibration error is less than 2%.

The PSD performance of the target cells is shown in Fig. 3. The energy dependence of the PSD is such that the two peaks become somewhat narrower and closer with higher energies. The valley of the PSD shifts slightly toward the γ (electron) peak as the energy gets larger. This effect is corrected for in the analysis. The high-energy neutron background is reduced by a factor 50 with a PSD cut.

^{3}He wire counters

Four large ^{3}He wire chambers, each with an outside dimension of 8 cm×88 cm×126 cm, were built. The sealed counters, each containing 80 l of pure (99.99%) ^{3}He gas at atmospheric pressure mixed with 1% of CO_2 quenching gas, are sandwiched between the target planes (Fig. 1). Special care was taken to choose materials with low natural radioactivities. The windows are 0.2-mm stainless-steel sheets. A single stainless-steel wire of 50 μm diameter is threaded through the chamber with a spacing of 2 cm.

The energy spectrum of a ^{3}He counter is shown in Fig. 4. The energy resolution at 765 keV (full energy peak) is about 25% FWHM for the best counter and 50% for the poorest one. The shoulder at the low-energy side is due to wall effects. The smallest possible signal of detection is 190 keV where the triton is accompanied by an escape proton. A hardware threshold is set at around 185 keV. The actual window used in the analysis is between 275 and 1340 keV. The background of each counter due to natural radioactivity is about 0.75 min^{-1} in this window. (The application of solder and glue inside the chambers was avoided.)

Veto tanks

The assembly of the target cells and of the ^{3}He counters is completely surrounded by six mechanically and optically independent liquid-scintillator planes, arranged in such a fashion that the radiation leaks between plane boundaries are small. Each tank, made out of aluminum, is 12 cm thick. The tanks are filled with the liquid scintillator NE235H. Each tank is provided with light reflectors. The reflectors on the large surfaces are lucite panels sealed on the edges to an aluminum sheet, thus providing an air gap allowing total reflection at the lucite-air interface. Two adjacent small faces are fitted with aluminum sheets coated with TiO_2 paint and sealed with thin lucite sheets. The two other small faces have lucite windows. The scintillation light is collected through these lucite windows by wavelength-shifter bars[30] coupled to two 7.5-cm photomultiplier tubes (Amperex XP2312). The wavelength-shifter bars are acrylic bars (16 mm thick) with 2 mg/l of BBQ (Ref. 28) concentration in which the blue scintillation light is absorbed and reemitted as isotropic green light propagating by total internal reflection to the end of the bar.

The six veto tanks are mounted on their movable transport system, rolling on two pairs of demountable tracks. The vertical front veto tank is attached to the horizontal bottom tank and constitutes a movable unit on which the target cells and the ^{3}He counters are installed, while the other four veto tanks form the second unit. This arrangement facilitates easy access to the central detector unit for calibration and maintenance.

The energy spectrum of the cosmic muons passing through the top veto tank is shown in Fig. 5.

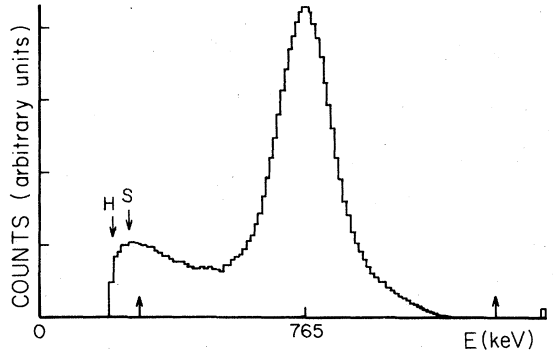

FIG. 4. The energy spectra of the ^{3}He counters. The hardware threshold is shown by the arrow (↓) with H. The software threshold set by a data-acquisition program is shown by the arrow (↓) with S. The energy window used in the analysis is shown by the arrow (↑).

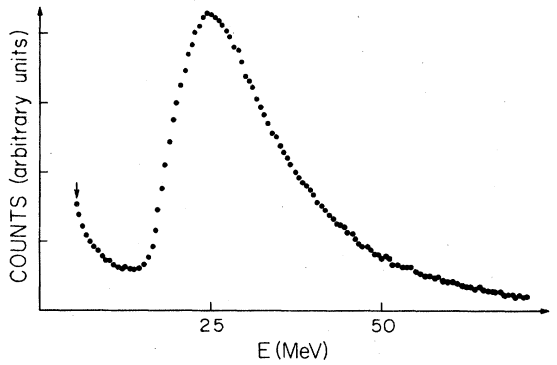

FIG. 5. Energy spectrum of the cosmic muons passing through the top veto tank. The arrow indicates the hardware threshold.

The hardware threshold is set so that the efficiency of the veto tanks in detecting cosmic muons is better than 99.8%.

The electronics for the veto pulse generate a 320-μs signal (long veto). ^{3}He events in coincidence with this signal are rejected. This 320-μs interval is a compromise between neutron rejection (it is about 95% efficient) and dead time (about 8%). A 10-μs signal is also generated for the anticoincidence with the target-cell events. It reduces the target-cell count rates above 2.5 MeV by a factor of 80.

The veto rejection efficiency for charged particles was better than 10^{-4}. This number is reduced further by redundancy requirements of the electronic system.

Umbrella veto

Four additional cosmic-ray veto scintillation counters are installed on top of the lead house (Fig. 1). They serve to suppress neutrons and electron bremsstrahlung coming from muons stopped in the upper part of the lead house. Each has 8 cm (thickness) $\times$ 130 cm $\times$ 150 cm outside dimension, and contains NE235H. Wavelength-shifter bars are placed on two narrow sides of the counter, while TiO_2 painted reflectors are provided with an air gap on the opposite sides. A 12.5-cm tube (Amperex XP1040) is used to view the bars.

A 10-μs signal is generated by the umbrella vetos, and is used in anticoincidence with the target-cell events. This reduces fast neutron events in the target cells by a factor of 2. In addition to the veto rejection, it further reduces the γ-ray rates above 2 MeV by 15%. Details of the effects of these veto anticoincidences are discussed below.

Shielding

A 20-cm-thick lead shield was chosen based on a measurement of the γ-ray radioactivities at the experimental site. Special low background lead was used for the inner part of the construction. The lead is supported in the inside by a 2-cm steel house. The 15-ton lead door moves on rollers and rails, so as to allow open access to the veto house.

On the inside of the steel house, 15-cm-thick polyethylene is used (Fig. 1) to moderate and capture neutrons. The 12-cm-thick veto tanks serve as additional absorbers.

Test measurements were performed with part of a 1-m concrete dividing wall removed, allowing some thermal neutrons from the reactor hall to reach the Pb house. These slow neutrons were captured in the lead and the steel, giving rise to high-energy γ rays, some of which in turn were detected by the target cells (above 4 MeV the rate was found increased by a factor 5). This extra accidental background was not significant, however, compared to the total background. It was observed that these slow neutrons did not increase the ^{3}He singles rates and the coincidence rates. It is concluded that there is no reactor-associated time-correlated background.

A total of 2.5 m of concrete shield over the detector eliminates most of the cosmic-ray nucleonic component and attenuates the muonic component.

Pressurized air is blown continuously into the veto house to keep out any radioactive gas, especially ^{41}Ar (1.29-MeV γ rays). This pressurized air, by passing through a copper coil immersed in a refrigerant at constant temperature, also serves to remove the heat generated by the photomultiplier tube bases and by the preamplifiers of the ^{3}He counters. As a result, the temperature of the detector system is maintained to ± 0.5 °C for each run.

Efficiency of the detector

The positron yield $Y(E_{e^+})$ is a function of the neutron detection efficiency and the positron response function, as well as of the finite size of the reactor core and of the detector. The neutron detection efficiency $\epsilon_n(t_w)$ depends on the coincidence time window t_w. The positron response function is $\epsilon_{e^+}(E_{\bar\nu}, E_{e^+}) = \eta(E_{\bar\nu}, E_{e^+}) A_{\rm PSD}$, where $\eta(E_{\bar\nu}, E_{e^+})$ gives the distortion of the positron spectrum caused by various effects and $A_{\rm PSD}$ is the acceptance of the PSD window. The positron yield is then [Eqs. (1) and (2)]

$$Y(E_{e^+}, \Delta^2 d, \theta) = N_p \epsilon_n(t_w) \int \phi(E_{\bar\nu}, \Delta^2 d', \theta) \sigma(E_{\bar\nu}) \epsilon_{e^+}(E_{\bar\nu}, E_{e^+}) \times h(d, d') dE_{\bar\nu} dd' , \quad (3)$$

where N_p is the number of the target protons, $\phi(E_{\bar\nu}, d)$ is the antineutrino spectrum at the detector ($=[N(E_{\bar\nu})/4\pi d^2] P(E_{\bar\nu}, \Delta^2 d, \theta)$ in the two-neutrino model), $\sigma(E_{\bar\nu})$ is the $\bar\nu_e p \to e^+ n$ cross section, with $E_{e^+} = E_{\bar\nu} - 1.8$ MeV, and $h(d, d')$ is the weighting factor of the distance d' ($d = 8.76$ m is the average distance). d' is the distance between the points of creation of a neutrino in the core and its absorption in the detector.

The neutron detection efficiency was measured using the MeV neutrons from an Am-Be source and keV neutrons from a Sb-Be source. It was also calculated using a neutron-transport computer program.[31]

With the Am-Be source, the energetic neutrons produce a signal in the target cells. If one counts

the single-neutron events in the target cell, identified as such by the PSD, and the coincidence events in a target cell and the adjacent ^{3}He counters, the ratio of the latter to the former gives the efficiency. After adding a 1% correction, calculated by a neutron-transport program, to correct for the difference between fast and slow neutrons, a value of $\epsilon_n(t=\infty) = 25.2 \pm 2.0\%$ was determined.

A spectrum of the time distribution between a fast-neutron prompt pulse in the target cell and a delayed pulse in the ^{3}He counter is shown in Fig. 6. This also shows the timing characteristic of the $\bar{\nu}_e p \to e^+ n$ reaction since MeV and keV neutrons take a similar time for thermalization. A 200-μs time window for the delayed coincidence, which gives an 80.1% acceptance, is used in the analysis as explained below. The neutron efficiency from the Am-Be measurement within this time window then becomes $\epsilon_n(200\ \mu s) = 20.2 \pm 1.6\%$.

The Sb-Be neutron source[32] is a calibrated ($\pm 3\%$) standard source. Its neutrons have energies of about 20 keV, comparable to those from inverse β decay. The active dimensions of this neutron source are 4 mm (diam) $\times$ 4 mm (long) encapsulated in a stainless-steel cylinder. The source was inserted into a specially built target cell which was substituted for any target cell within the detector array. Within the cell the source could be moved in three dimensions, with 2-mm precision, using stepping motors. Fifty-six different source positions and three target-cell positions were mapped. Each point was measured to about 2% statistical error.

Because of the high γ-ray flux from this source, the software threshold was set higher than in the analysis. The resulting correction was measured using an Am-Li source (mean energy about 500 keV) in various positions. This relative correction, which varies between 12 and 15%, was applied in the efficiency calculation.

The variation of the efficiency along the 9-cm target-cell width, using one ^{3}He counter only, is shown in Fig. 7. As can be seen, the efficiency varies almost linearly with the distance. For the central target cells, the neutron can be detected in the ^{3}He counter on either side, and the contribution from each side has to be summed. The resulting efficiency becomes a constant over the whole width. Only a small fraction (less than 0.5%) of the neutrons will end up in a nonadjacent ^{3}He counter. The efficiency as a function of the position in the target cell is shown in Fig. 8. The efficiency remains constant over a wide range and drops off at the edge.

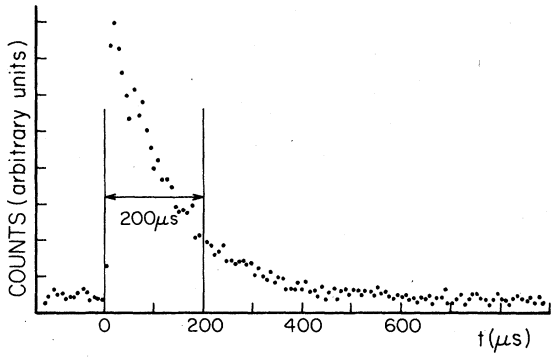

FIG. 6. Spectrum of the time distribution between a fast-neutron prompt pulse in the target cell and a delayed pulse in the ^{3}He counter. The 200-μs time window is used in the analysis.

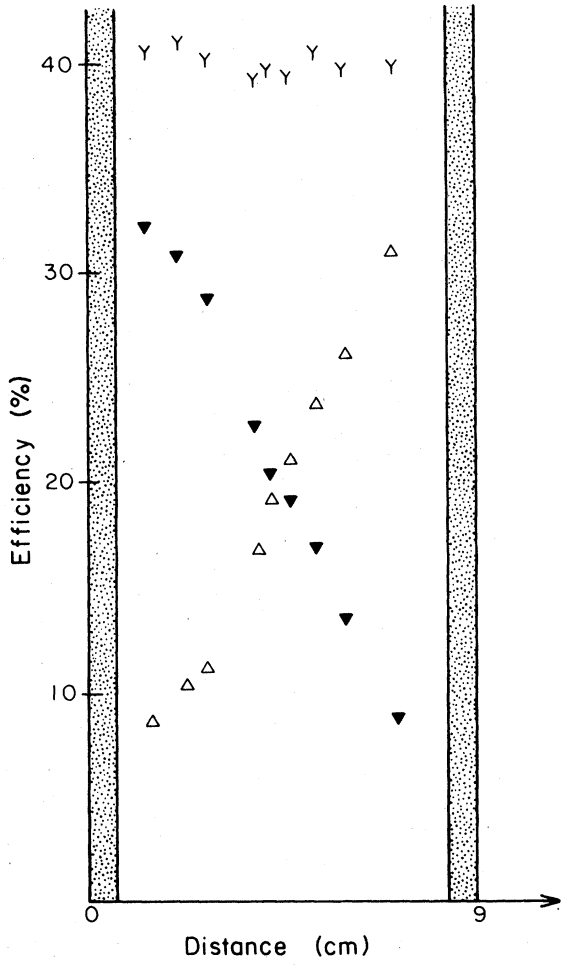

FIG. 7. Variation of the neutron detection efficiency along the target-cell width showing ▼ (efficiency for the left ^{3}He counter), △ (efficiency for the right ^{3}He counter), *Y* (the sum of the left and right counters). The lucite walls are illustrated as a dotted area.

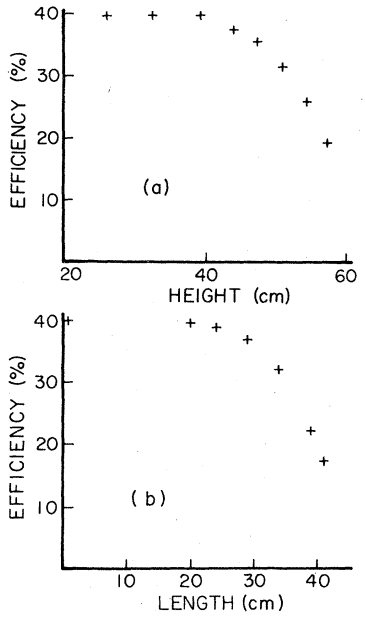

FIG. 8. Variation of the neutron detection efficiency along the vertical axis [height, Fig. 8(a)] and the horizontal axis [length, Fig. 8(b)] of the target-cell plane (containing six target cells), using the ^{3}He counters on both sides. The distances are given with reference to the center of the target-cell plane.

To calculate the overall neutron-detection efficiency, the target cells are divided into four groups (A to D) according to their positions as shown below. The efficiency of the target cells in each group is identical and depends on whether the neutrons can escape the detector along the length, height, or width of the cells. The efficiencies for each group can be written as follows (see Fig. 1):

$$\epsilon_A = \epsilon_0\eta_L, \quad A = 2,2;\ 2,3;\ 2,4;\ 2,5;\ 3,4;\ 3,5;\ 3,6;\ 3,1;\ 4,6;\ 4,1;\ 4,2;\ 4,3,$$

$$\epsilon_B = \epsilon_0\eta_L\eta_H, \quad B = 2,1;\ 3,3;\ 4,5;\ 2,6;\ 3,2;\ 4,4,$$

$$\epsilon_C = \epsilon_0\eta_L\eta_W, \quad C = 1,6;\ 1,1;\ 1,2;\ 1,3;\ 5,2;\ 5,3;\ 5,4;\ 5,5,$$

$$\epsilon_D = \epsilon_0\eta_L\eta_H\eta_W, \quad D = 1,5;\ 5,1;\ 1,4;\ 5,6,$$

where ϵ_0 is the efficiency for the center of the target cell and η_L, η_H, η_W are the correction factors for the length, height, and width, respectively, of the target cell. These efficiency values are obtained from the results shown in Figs. 7 and 8 and are given by $\epsilon_0 = 0.40 \pm 0.014$, $\eta_L = 0.87 \pm 0.02$, $\eta_H = 0.75 \pm 0.03$, $\eta_W = 0.50 \pm 0.04$. Then the overall efficiency is obtained as follows (error is systematic error):

$$\bar{\epsilon} = \tfrac{1}{30}\,(12\epsilon_A + 6\epsilon_B + 8\epsilon_C + 4\epsilon_D) = (25.6 \pm 2.0)\%.$$

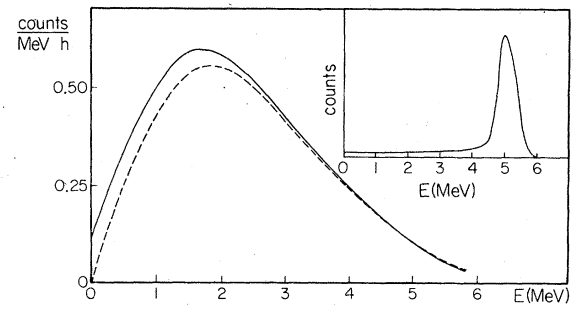

FIG. 9. Positron energy spectrum before (dashed curve) and after (solid curve) application of the positron detection response $\eta\,(E_{\bar{\nu}}, E_{e^+})$. The insert illustrates the response of the detector to monoenergetic 5-MeV positrons.

It should be noted that only the ^{3}He counters adjacent to plane 4 (Fig. 1) were used in the efficiency measurement. An additional correction obtained from measuring the integral count rate with a neutron source in two symmetric positions has been applied to the ^{3}He counters facing plane 2. The efficiency in the ^{3}He energy window finally obtained is $\epsilon(t_w = \infty) = 24.3 \pm 2.0$.

The efficiency within 200-μs coincidence window is then given by $\epsilon(200\ \mu\text{s}) = 19.4 \pm 1.7\%$. This value has been used in the subsequent analysis.

The *positron-detection response* $\eta(E_{\bar{\nu}}, E_{e^+})$ was calculated with a Monte Carlo program. The positron yield without the response correction, $\sigma(E_{\bar{\nu}})N_p\phi\,(E_{\bar{\nu}})\epsilon_n(t_w)A_{\text{PSD}}$, is shown as a dotted line in Fig. 9. The acceptance A_{PSD} of the PSD window used in the final analysis is 98%. Using this raw spectrum, the program calculates the deformation due to the effect of the finite range of the positron, the 0.511-MeV annihilation γ rays, the energy resolution of the detector, and the antineutrinos interacting in the lucite. The resulting positron spectrum $Y(E_{e^+})$ is shown with a solid line in Fig. 9. The distortion is not very significant.

Data acquisition

The electronic scheme consists of circuits for the target cells, the ^{3}He counters, the vetos, and the umbrellas. The analyzed signals enter the CAMAC system which communicates with a PDP 11/40 computer. Data are stored in the computer memory by an on-line program and also written on magnetic tapes for final off-line analysis.

The signals from four photomultiplier tubes of each target cell are passively added together. The 30 target cells labeled by i, k in (Fig. 1) are arranged into five vertical planes ($i = 1$ to 5) and into six groups ($k = 1$ to 6). The energy signals from the same group but different planes are fanned-in together (to reduce the number of elec-

tronic modules). This particular method of fanning-in minimizes the solid angle for the possible accumulation of the 0.511-MeV annihilation γ rays in the same group of target cells. The energy and the PSD signals from the target cells are analyzed by an analog-to-digital converter (ADC). The 12-channel ADC of 9 bits is charge sensitive with a dead time of 9 μs. The digitized signals of each channel are incrementally stored in its own 32-word buffered memory. When the memory is full, it is cleared and a new sequence begins.

Each signal from a target cell above the hardware threshold sets a bit in a TAG unit and records the time in a TIMER unit. Both the TAG and the TIMER unit have 32 word memories which cycle continuously and synchronously with the target-cell ADC. Thus the time and the TAG pattern of the previous target cell events are always available.

The TAG unit uses 47 bits (30 for the target cells, 4 for the ^{3}He counters, 6 for the veto tanks, 4 for the umbrellas, and 3 special veto bits), which identify the detector modules. With the TIMER and the TAG information an event can be reconstructed indicating when and where it occurred.

The signals from each ^{3}He counter are shaped and amplified and then analyzed in the ^{3}He ADC (peak sensing, 11 bits), with each counter having its own channel. The ^{3}He signals set a bit in the TAG, and record the time in the TIMER. They also generate a LAM in the CAMAC system.

Each veto or umbrella pulse above the hardware threshold sets its own bit in the TAG. However, this does not cause the TAG memory to increment. The energies of the vetos and the umbrellas are analyzed in their own ADC, but are not used in the normal data-acquisition mode. They are used in the calibration of the vetos and umbrellas, along with the TAG information.

The cosmic-ray anticoincidences are not hardwired. Instead, three special bits are provided in the TAG unit for the vetos and the umbrellas. A veto tank signal above the hardware threshold generates a short veto signal (10 μs) and a long veto signal (320 μs) which are set at the input of the identification TAG. In the same manner, an umbrella event generates a short umbrella signal (10 μs). The corresponding special veto bits are set in the TAG memory whenever a target-cell event or a ^{3}He event occurs while these signals are on. These special veto bits are used for the anticoincidences in the analysis.

With the electronics setup sketched above and documented in detail in Ref. 33, the data acquisition works as follows:

(1) A signal from a ^{3}He counter above the hardware threshold (set just above the noise level indicated by arrows in Fig. 4) generates a LAM signal to the CAMAC, which triggers a computer interruption. The time, the TAG, and the energy of the ^{3}He event are read into the computer.

(2) If the ^{3}He event is above the software energy threshold, the information from three preceding target-cell events is then read and stored into the computer memory. The idea is that by using the second and the third previous events, the accidental background can be measured "on-line". This also allows the possibility of studying the stability of the system and the correlated background.

(3) Data are written on a magnetic tape for the off-line analysis. The on-line program monitors the system and analyzes the data while the experiment is running.

An "event" consists of a ^{3}He event with three previous target-cell events. The raw data recorded on the tapes are: time, TAG, and energy of a ^{3}He event as well as time, TAG, energy, and PSD of three preceding target-cell events.

The rate of "events" is about 25 min^{-1}. With this rate, a 2400-ft magnetic tape is filled in three days. This time period constitutes a "run". Between two runs, system checks are made as described below.

After each run, an Am-Be source is inserted inside the lead house for the energy calibrations of the detector. The Compton edge of the 4.439-MeV γ ray in ^{12}C* is used to check the gain of each target cell. If necesary the gain is reset to the nominal value by adjusting the high voltage of the respective phototube. Simultaneously the neutrons from the Am-Be source are used for the calibration of each ^{3}He counter. The vetos and umbrellas are calibrated with the cosmic-ray muon spectrum.

Various singles rates of the detector components are monitored with the on-line program during the measurements, and are shown in Table I. It should be noted that the singles rates of the target cells and the ^{3}He counters are essentially reactor independent. During the calibrations, it was observed that the gain shift of the target cells was less than 1%. Data collected for 3088.7 h (live time) with reactor on, and 1181.8 h (live time) with reactor off.

Dead time was measured, using a pulser, to be 15.5 and 20.0% for reactor off and on, respectively. The difference is due to the high rate in the umbrellas for reactor on.

Data reduction

The mean time interval between the target-cell single events is 4.5 ms (at a target-cell singles

TABLE I. The count rates of the detector components sampled before and during the full power operation of the reactor. These figures are 1% accurate, except for the umbrella rates reactor on, which are 5% accurate.

Reactor status	Count rates (s^{-1}) 30 target cells[a]	4 ^{3}He counters[b]	6 veto tanks[a]	4 umbrellas[a]
Off	216.3	0.422	256.8	440
On	216.7	0.427	258.6	5384

[a]Counts above the hardware threshold.
[b]Counts above the software threshold ("event" rates).

rate of 220 s^{-1}), whereas the time window for recording a neutrino event is about 200 μs (Fig. 6). Consequently, only the first target-cell event preceding the ^{3}He event is considered to be a candidate for a neutrino event.

Various conditions are imposed to suppress backgrounds originating from various sources. The selection of the good events is made as follows.

(1) Reject the first previous target-cell event if it occurred in more than one cell. This is meant to reject cosmic-ray-related events and a possible Compton scattering of high-energy bremsstrahlung.

(2) Reject a multi-^{3}He event since there is only one neutron created by a neutrino event. These events are rare (0.05 min^{-1}).

(3) Reject a ^{3}He event outside the energy window, to suppress the γ-ray background and the electronic noise at low energy and the α-background at high energy. This condition reduces the total ^{3}He counting rate from 25 min^{-1} (the rate of the data acquisition) to 11 min^{-1}. Most of the eliminated events are due to α activity in the ^{3}He counters.

(4) Reject a ^{3}He event occurring in a plane not adjacent to the plane of the first previous target-cell event. This condition cuts down the accidental background by a factor of 2.5 as can be seen from a geometrical argument. This condition can be imposed since the neutrons created in the reaction cannot travel far without being absorbed as mentioned above.

(5) Reject a ^{3}He event which is in coincidence with the long veto (320 μs). This rejects the neutrons created in the shielding and in the detector by cosmic rays which diffuse into the system, and cuts the total ^{3}He counting rate from 11 to 4 min^{-1}.

(6) Reject the first previous target-cell event in coincidence with a short veto or a short umbrella signal (10 μs). This suppresses the bremsstrahlung events caused by decay electrons of cosmic muons stopped in the shielding. For correlated neutron—γ-ray events, this overlaps the long-veto rejection. The umbrella-event rejection alone reduces the fast-neutron rate by a factor of 2.

(7) Reject a ^{3}He event which comes more than 200 μs after the target-cell event. This is the time window used in the analysis which accepts 80.1% of the neutrino-induced events. This window is a compromise between good efficiency and signal-to-background ratio. A 300-μs window will accept 94% of the events but the accidental background will increase by 50%.

(8) Reject an event if the two previous target cell-events are separated by less than 300 μs. This condition was first imposed since it would not be known which of the two was the positron event. It was found later that this condition reduces the background below 2 MeV by a factor of 2. From the study of the double and the triple target-cell events in coincidence with a ^{3}He event, the energy spectrum of those rejected events shows a Compton edge around 2.0 MeV from neutron capture on protons. These events are caused presumably by multiple-neutron events created by cosmic rays in the shielding. For example, two neutrons are captured by protons in the target cells creating 2.2-MeV γ rays while a third one enters the ^{3}He counter.

(9) Reject neutron (recoil-proton) events of the first previous target-cell events using the PSD. As the valley of the PSD slightly depends on the energy, the PSD spectrum of each target cell is fitted as a function of the energy and shifted accordingly to bring the valleys to the same position independent of energy. The PSD cut is made so that the acceptance of the positron event, A(PSD), is 98%.

The rejection efficiencies of some of the important cuts are shown in Table II.

After imposing the conditions (1)—(8), a two-dimensional energy-PSD spectrum is constructed from the data. The PSD spectra for a given energy region are shown in Fig. 10. The areas under the neutron peak are the same for reactor on and reactor off demonstrating that there are no reactor-associated fast neutrons, whereas the area

TABLE II. Event rates in h^{-1} for various cuts illustrating the rejection efficiencies. The rejection conditions are shown by 1 (imposed) or 0 (relaxed). The symbols are adj = adjacency requirement, condition (4) in the text; T_{12} = 300-μs veto for target-cell events, condition (8) in the text; V_L = 320-μs long veto for ^{3}He events, condition (5) in the text; V_S = 10-μs short veto for target-cell events, condition (6) in the text; and U_S = 10-μs short *umbrella* only for target-cell events, condition (6) in the text.

	Rejection conditions					Dead	γ-ray energy range				Neutrons
	adj	T_{12}	V_L	V_S	U_S	time (%)	1.0–1.3 MeV	1.3–2.2 MeV	2.2–4.2 MeV	4.2–8.8 MeV	1.3–8.8 MeV
Reactor off	1	1	1	1	1	15.5	0.84(4)	1.05(4)	0.47(3)	0.32(2)	4.63(9)
715.516 h	1	1	1	1	0	15.0	0.95(4)	1.21(4)	0.65(3)	0.44(3)	6.89(11)
real time	1	1	0	1	1	6.7	1.16(4)	1.66(5)	0.59(3)	0.37(2)	4.47(8)
	1	0	1	1	1	8.4	1.07(4)	1.55(5)	0.57(3)	0.38(2)	4.50(8)
	0	1	1	1	1	15.5	1.94(6)	2.08(6)	0.83(4)	0.47(3)	5.63(10)
	1	1	0	0	1	6.7	1.83(5)	2.79(6)	1.68(5)	1.29(4)	8.79(11)
	1	1	0	0	0	7.2	3.07(7)	4.55(8)	3.46(7)	2.95(7)	16.17(16)
Reactor on	1	1	1	1	1	20.0	1.04(4)	1.54(5)	1.20(4)	0.43(3)	4.65(8)
843.55 h	1	1	1	1	0	15.0	1.10(4)	1.68(5)	1.34(4)	0.56(3)	7.08(10)
real time	1	1	0	1	1	11.7	1.38(4)	2.16(5)	1.29(4)	0.46(3)	4.52(8)
	1	0	1	1	1	13.4	1.29(4)	2.12(5)	1.30(4)	0.49(3)	4.54(8)

under the γ (electron or positron) peak is clearly enhanced for reactor on due to antineutrino events.

The energy spectra for reactor on and reactor off are obtained by rejecting the events under the neutron peak [condition (9)], and are shown in Fig. 11. These spectra are dead-time corrected.

Stability checks

The ^{3}He single rates (within the energy window) with a long-veto (320 μs) anticoincidence are shown in the third column of Table III. When the reactor is on, there are an estimared 5 ± 1 h^{-1} more counts in the ^{3}He counters due to neutrons from neutrino-induced events in the target cells and the veto tanks. This rate has been subtracted from the reactor-on rates in the third column of the Table III. The examination of the reactor-on and reactor-off data shows that the stability of the ^{3}He counters is better than 1%. In total, the count rates for reactor on and reactor off differ by (0.4 ± 0.8)%. If this is interpreted as reactor-associated single-neutron events, this could increase the accidental background by that amount.

The fourth column of Table III shows the ^{3}He singles rates in coincidence with the long veto [rejected by long veto in the analysis, condition (5)]. These are the neutrons related to the cosmic rays. No change is seen whether the reactor is on or off.

The target-cell singles rates are much higher

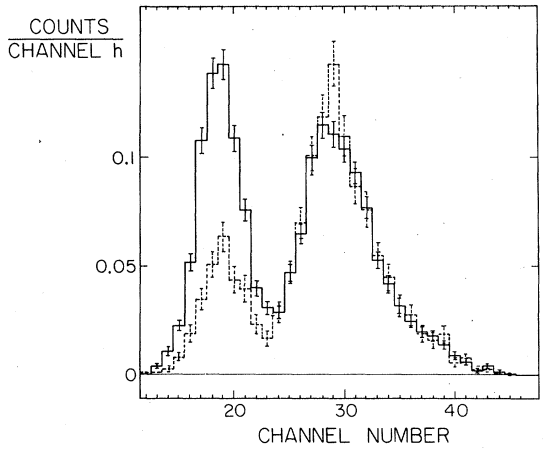

FIG. 10. PSD spectra for reactor off (dashed line) and reactor on (solid line) for 2.7–4.2 MeV. For reactor on the γ-e^+ peak is enhanced due to neutrino-induced positrons. The areas under the neutron peak are the same for reactor on and reactor off.

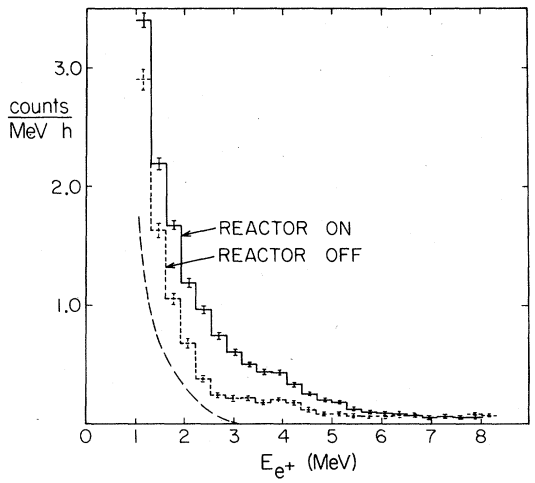

FIG. 11. Positron energy spectra for reactor on (3088.7 h live time) and reactor off (1181.8 h live time). The accidental background is shown as a dashed line.

TABLE III. Rates of the ^{3}He counters and the target cells. The symbol V_L means a 320-μs long-veto signal as explained in the text. Target-cell events between 1 and 7 ms after a ^{3}He count in anticoincidence with V_L are accepted. The errors are statistical errors only. The reactor-on entries are corrected for the neutrino-induced neutrons (5 ± 1 counts/h). The data is illustrative of the system stability.

Reactor status	Data taking (real time in h)	^{3}He count rates (h^{-1}) anticoinc. with V_L	coinc. with V_L	Target-cell count rates (h^{-1}) 1.0–1.3 MeV	1.3–2.7 MeV
Off	291.52	245.96(92)	439.31(1.23)	42.04(40)	34.85(36)
On	639.07	246.75(63)	434.85(82)	42.02(27)	34.66(25)
Off	202.63	244.22(1.10)	433.17(1.46)	38.51(46)	32.85(42)
On	584.73	250.51(66)	437.80(87)	39.07(27)	33.23(25)
Off	221.37	248.69(1.06)	428.59(1.39)	38.79(44)	32.98(40)
On	471.75	250.97(74)	438.76(96)	37.53(30)	32.43(28)
Off	254.75	245.40(98)	432.60(1.30)	38.33(41)	33.95(38)
On	823.07	247.03(55)	427.48(72)	39.64(23)	34.77(22)
Off	223.10	245.37(1.05)	422.82(1.38)	37.50(43)	32.28(40)
On	806.01	245.61(56)	421.62(72)	39.60(23)	34.14(22)
Off	91.64	244.27(1.63)	431.54(2.17)	37.40(67)	32.18(62)
On	298.17	243.09(91)	443.82(1.22)	39.54(39)	34.09(36)
On	238.10[a]	248.56(1.03)[a]	385.18(1.27)[a]	40.31(44)[a]	35.42(41)[a]
Off	113.57[a]	252.45(1.49)[a]	387.51(1.85)[a]	39.81(62)[a]	33.86(57)[a]
Total reactor on	3860.89	247.46(26)	428.63(33)	39.67(11)	34.07(10)
Total reactor off	1398.58	246.34(42)	427.72(55)	39.07(18)	33.41(16)
Total on – off		1.12(49)	0.91(65)	0.61(21)	0.66(19)

[a]For these measurements, the efficiency of the He chambers was increased by 5.7%. The entries were corrected for this. The average values are mentioned throughout the text. Also, the chambers were less sensitive to cosmic rays.

than the ^{3}He rates (Table I, third column). The steep energy spectrum of the singles in the target cell (Fig. 11) is used to test the stability of the detector and the electronics. Target-cell events arriving between 1 and 7 ms before the ^{3}He event are considered. Except for this time window and the condition (8), all other standard cuts are made. The spectrum obtained here has good statistical accuracy. It is sensitive to the gain shift of the target cells, to the rates of the ^{3}He counters, the vetos and the umbrellas, and to the stability of the electronics. It monitors the steep accidental background.

The fifth and the sixth column of the Table III show these target-cell event rates for two different energy bins. Since these rates are proportional to the ^{3}He count rates, they were corrected for the neutrino-induced neutrons when the reactor was on (2% correction).

It is shown that the accidental background is stable to $\pm 2\%$. As a whole, the reactor-on and reactor-off spectra differ by less than 2%.

It is concluded that the detector is stable to within 2%. Given the good signal-to-background ratio, this does not lead to any significant uncertainty on the positron spectrum.

Background

From the discussions of the previous section, there is no significant reactor-associated accidental background (less than 1% of the total background).

The last column of the Table II shows that the fast neutron events (events which are discriminated by the PSD) are the same for reactor on and reactor off. This can also be seen from Fig. 10, demonstrating that there are no fast neutron events associated with the reactor. From the result of the differential shielding test, it is concluded that there are no slow neutrons which can give rise to a correlated event. Thus it is concluded that there is no significant reactor-associated background.

The reactor-independent background measured during the reactor-off periods is the only significant background in this experiment. The result of the measurement is shown in Fig. 11, with the accidental component given by a dotted line. An important contribution to the accidentals can be attributed to the ^{40}K contamination (1.46-MeV γ rays) from the glass of the photomultiplier tubes. The background above 3 MeV is due entirely to time-correlated cosmic-ray events.

III. RESULTS AND DISCUSSION

In this section, the experimental positron spectrum is obtained and analyzed in terms of the parameters of neutrino oscillations.

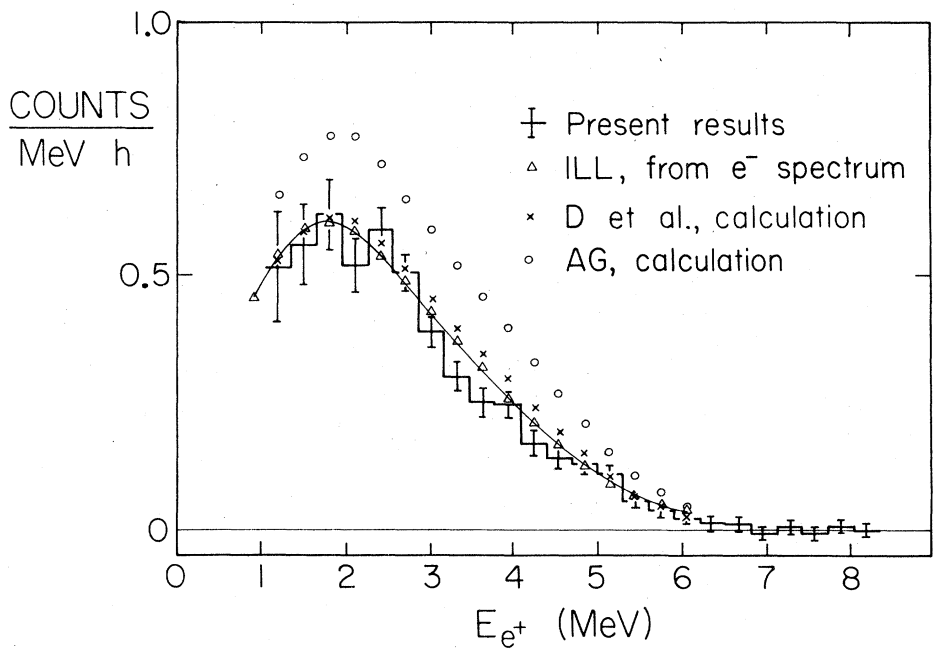

FIG. 12. Positron energy spectrum. The solid curve represents the expected positron spectrum based on the ILL electron-spectrum measurement. The calculated spectra AG (Ref. 26) and D *et al.* (Ref. 22) are also shown. No errors are indicated.

Experimental positron spectrum

The experimental positron energy spectrum is obtained by subtracting the reactor-off spectrum from the reactor-on spectrum. This spectrum is shown in Table IV and Fig. 12 with statistical errors only. The signal-to-background ratio is 1:1 at 2 MeV and better above that energy. In total, 4890 ± 180 neutrino-induced events have been detected with a counting rate of (1.58 ± 0.06) h^{-1} (live time) for $E_{e^+} > 1$ MeV.

The expected positron spectrum for no oscillation is also plotted in Fig. 12. This spectrum is based on the on-line electron spectrum experiment of Ref. 23 as discussed above.

Systematic errors affecting the positron spectrum are summarized as follows: (1) the uncertainty in the normalization of the intensity of the antineutrino energy spectrum (6.5%); (2) the uncertainty in the detection efficiency (8%); (3) the uncertainty in the inverse-β-decay cross section (neutron lifetime) (1.2%); (4) the uncertainty in the energy release per fission (1%); (5) the instability of the reactor power (less than 1%); (6) all other uncertainties (less than 2%).

Thus, there is a resulting 11% total systematic error which is essentially energy independent. In addition, a possible distortion of the spectrum associated with a 2% energy calibration uncertainty must be taken into account.

Results and discussions

The ratio of the experimental to expected integral positron yield for $E_{e^+} > 1$ MeV was found to be

$$\frac{\int Y_{\text{exp}}(E_{e^+})dE_{e^+}}{\int Y_{\text{no osc}}(E_{e^+})dE_{e^+}} = 0.955 \pm 0.035(\text{statistical})$$

$$\pm 0.11 \text{ (systematic)}.$$

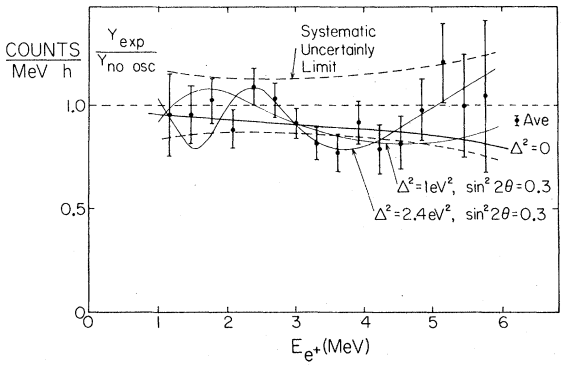

FIG. 13. The ratio of the experimental to the theoretical positron yield. The errors shown with data points are statistical errors only. The systematic errors are given by the dotted bands as explained in the text. For each set of Δ^2 and $\sin^2 2\theta$ the normalization and gain were varied, within their uncertainties, to find the lowest values of χ^2. Three curves corresponding to the indicated sets of parameters are shown.

TABLE IV. Experimental positron spectrum $Y_{exp}(E_{e^+})$ and expected spectrum for no oscillations $Y_{no\ osc}(E_{e^+})$.

E_{e^+} [a] (MeV)	$Y_{no\ osc}(E_{e^+})$ [b] ($MeV^{-1}\ h^{-1}$)	$Y_{exp}(E_{e^+})$ [c] ($MeV^{-1}\ h^{-1}$)
1.182	0.540	0.515(109)
1.487	0.589	0.562(83)
1.792	0.604	0.620(69)
2.097	0.585	0.517(56)
2.402	0.544	0.593(45)
2.707	0.488	0.503(37)
3.012	0.428	0.391(31)
3.317	0.370	0.301(29)
3.622	0.318	0.246(28)
3.927	0.265	0.243(28)
4.232	0.214	0.169(26)
4.537	0.170	0.139(22)
4.842	0.129	0.126(19)
5.147	0.091	0.110(17)
5.452	0.061	0.061(15)
5.757	0.038	0.040(14)
6.062		0.025(13)
6.367		0.014(14)
6.672		0.015(13)
6.977		−0.004(13)
7.282		0.005(13)
7.587		−0.003(13)
>1.0	1.657 [d]	1.583(58) [d]

[a] Channel width 0.305 MeV.

[b] Predicted e^+ spectrum, assuming no oscillations, from electron-spectrum measurements (Ref. 23).

[c] Experimental e^+ spectrum at $d = 8.76$ m. The statistical errors are given (68% C.L.).

[d] Integral rate per h for $E_{e^+} > 1$ MeV.

The ratio $Y_{exp}(E_{e^+})/Y_{no\ osc}(E_{e^+})$ of the experimental positron spectrum to the expected one assuming no oscillation is plotted in Fig. 13. This is to be compared with the corresponding ratio based on Eq. (3),

$$R(E_{e^+}) = \frac{Y(E_{e^+}, d\Delta^2, \theta)}{Y_{no\ osc}(E_{e^+})}. \quad (4)$$

A χ^2 test of $R(E_{e^+})$ as a function of Δ^2 and $\sin^2 2\theta$ was performed to the data of the Fig. 13. The 11% uncertainty in the normalization and the 2% uncertainty in the energy scale can lead to distortions of the oscillation function. All the values within these limits are assumed to be equally probable. Therefore, for each set of Δ^2 and $\sin^2 2\theta$, the normalization and gain were varied, within their uncertainties, to find the lowest values of χ^2. These values, normalized with regard to the two mentioned free parameters, were used to determine the confidence limits in the Δ^2 vs $\sin^2 2\theta$ plane depicted in Fig. 14 where the 68% and 90% confidence limits are shown. The regions to the left of the curves are allowed.

The experimental data are consistent with no oscillations. At maximum mixing, a limit of $\Delta^2 \leq 0.15$ eV^2 (90% C.L.) is found. For small mixing angles, various solutions are possible, including those shown as examples in Fig. 13. For very large values of Δ^2 ($\gtrsim 20$ eV^2), owing to the fine resolution, our data are sensitive to $\sin^2 2\theta$ only. This leads to an upper limit of $\sin^2 2\theta < 0.32$ (90% C.L.). The capes in Fig. 14 at 1.0, 2.4, and 3.7 eV^2 stem from the low points between 3 and 4 MeV in our data (Fig. 13). A preliminary account of this work has been presented in Ref. 34.

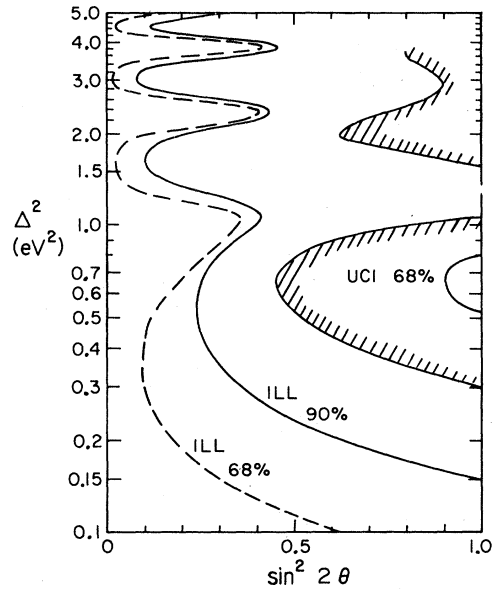

FIG. 14. The limits on the neutrino-oscillation parameters Δ^2 versus $\sin^2 2\theta$ given by the present experiment for 68% and 90% confidence level (C.L.). The regions to the right of the curve can be excluded. The allowed regions proposed in Ref. 17 are shown as a shaded area contained by the curves labeled UCI.

For comparison, the results published by Reines *et al.*[17] based on a study of the reaction yield $\bar{\nu}_e d \to e^+ nn$ and $\bar{\nu}_e d \to \bar{\nu}_e pn$ at 11.2 m from the reactor core are also shown in Fig. 14. At the closest point the 68%-confidence-limit results of Reines *et al.* are about 1.5 standard derivation from our 90% confidence limit.

Experimental upper limits on oscillation parameters from studies of other channels,[16] in particular from the channel $\nu_\mu \to \nu_e$,[19] are considerably larger and thus not inconsistent with the present findings.

Conclusion

The present experiment furnishes stringent limits on the neutrino-oscillation parameters Δ^2 and $\sin^2 2\theta$. The results are consistent with no oscillations, or with oscillations with a small

mixing angle.

A continuation of this experiment is in progress with improved background conditions. Data will be taken at two or more different positions from the core of the Gösgen[35] and Bugey[36] reactors. A sensitivity of $\Delta^2 < 0.01$ eV^2 for full mixing and $\sin^2 2\theta < 0.15$ should be attainable with the experiment[35] in the near future.

ACKNOWLEDGMENTS

The authors wish to thank the ILL for its generous hospitality and support. C. Bouton, C. Barnoux, and B. Guerre Chaley have participated in the construction of the detector. W. Mampe's help in planning the experiment is appreciated. Stimulating discussions with B. Davis, P. Ramond, F. Reines, K. Schreckenbach, H. Sobel, and V. Zacek are gratefully acknowledged. The continuous advice and help by P. Vogel has been invaluable. H. Fritzsch and P. Minkowski, who sparked these investigations during their visit to Caltech in 1975, have provided us with much encouragement. Part of this work constitutes the Ph.D. thesis of H. Kwon. Financial support was provided by the U.S. Department of Energy through Contract No. DE-AC-03-76ER00063, the Alfred P, Sloan Foundation, the Bundesministerium für Forschung and Technologie of the Federal Republic of Germany, and by the Institut National de Physique Nucléaire et Physique des Particules of France. F. Boehm is grateful for an award from the Humboldt Foundation. A. A. Hahn has profitted from a cooperative NSF-CNRS grant.

---

*Current address: SIN, CH-5234 Villigen, Switzerland.

[1]B. Pontecorvo, Zh. Eksp. Teor. Fiz. 34, 247 (1958) [Sov. Phys.—JETP 7, 172 (1958)].

[2]M. Nakagawa *et al.*, Prog. Theor. Phys. 30, 727 (1963); Y. Katayama *et al.*, *ibid.* 28, 675 (1962); Z. Maki *et al.*, *ibid.* 28, 870 (1962).

[3]V. Gribov and B. Pontecorvo, Phys. Lett. 28B, 493 (1969).

[4]A review about solar neutrinos can be found in J. N. Bahcall, Rev. Mod. Phys. 50, 881 (1978) and references therein.

[5]H. Fritzsch, in *Fundamental Physics with Reactor Neutrons and Neutrinos*, edited by T. von Egidy (Hilger, London, 1978), p. 117.

[6]S. M. Bilenky and B. Pontecorvo, Phys. Report 41, 225 (1978). Neutrino oscillations were discussed by various authors: L. Wolfenstein, Phys. Rev. D 20, 2634 (1979); J. N. Bahcall and H. Primakoff, *ibid.* 18, 3463 (1978); H. Fritzsch and P. Minkowski, Phys. Lett. 62B, 72 (1976); S. M. Bilenky and B. Pontecorvo, *ibid.* 61B, 248 (1976); S. Eliezer and A. R. Swift, Nucl. Phys. B105, 45 (1976); S. Eliezer and D. A. Ross, Phys. Rev. D 10, 3088 (1974); J. N. Bahcall and S. C. Frautschi, Phys. Lett. 29B, 623 (1969).

[7]Neutrino masses in the grand unification theories are discussed in M. Magg and Ch. Wetterich, Phys. Lett. 94B, 61 (1980); A. Zee, *ibid.* 93B, 389 (1980); E. Witten, *ibid.* 91B, 81 (1980); R. Barberi *et al.*, *ibid.* 90B, 91 (1980); 90B, 249 (1980); R. N. Mohapatra and G. Senjanovic, Phys. Rev. Lett. 44, 912 (1980); R. N. Mohapatra and R. E. Marshak, *ibid.* 44, 1316 (1980).

[8]S. Glashow, Nucl. Phys. 22, 22 (1961); A. Salam and J. Ward, Phys. Lett. 13, 168 (1964); S. Weinberg, Phys. Rev. Lett. 19, 1264 (1967).

[9]E. F. Tretyakov *et al.*, Izv. Akad. Nauk SSSR Ser. Fiz. 40, 20 (1976).

[10]M. Daum *et al.*, Phys. Lett. 74B, 126 (1978).

[11]W. Bacino *et al.*, Phys. Rev. Lett. 42, 749 (1979).

[12]V. A. Lyubimov *et al.*, Phys. Lett. 94B, 266 (1980).

[13]R. Cowsik and J. McClelland, Phys. Rev. Lett. 29, 669 (1972); B. W. Lee and S. Weinberg, *ibid.* 39, 165 (1977); P. Hut and K. A. Olive, Phys. Lett. 87B, 144 (1979).

[14]D. Schramm and G. Steigman, Phys. Lett. 87B, 141 (1979).

[15]S. Weinberg, in *Neutrinos—78*, proceedings of the International Conference on Neutrino Physics and Astrophysics, Purdue Univ., 1978, edited by E. C. Fowler (Purdue Univ., West Lafayette, Indiana, 1978).

[16]F. Boehm, in *Neutrinos—80*, proceedings of the International Conference on Neutrino Physics and Astrophysics, Erice, 1980, edited by E. Fiorini (Plenum, New York, 1981).

[17]F. Reines, H. W. Sobel, and E. Pasierb, Phys. Rev. Lett. 45, 1307 (1980).

[18]A. De Rújula *et al.*, Nucl. Phys. B168, 54 (1980).

[19]S. E. Willis *et al.*, Phys. Rev. Lett. 44, 522 (1980).

[20]F. A. Nezrick and F. Reines, Phys. Rev. 142, 852 (1966).

[21]C. J. Christensen *et al.*, Phys. Rev. D 5, 1628 (1972); J. Byrne *et al.*, Phys. Lett. 92B, 274 (1980).

[22]B. R. Davis, P. Vogel, F. M. Mann, and R. E. Schenter, Phys. Rev. C 19, 2259 (1979).

[23]*Reactor Handbook*, 2nd ed. (Interscience, New York, 1962), Vol. 3.

[24]K. Schreckenbach *et al.*, Phys. Lett. 99B, 251 (1981).

[25]J. K. Dickens *et al.*, Nucl. Sci. Eng. 74, 106 (1980).

[26]F. T. Avignone III and Z. D. Greenwood, Phys. Rev. C 22, 594 (1980).

[27]See, for example, F. D. Brooks, Nucl. Instrum. Methods 162, 477 (1979).

[28]Charles Hurlbut, Nuclear Enterprises, Inc., San Carlos, California 94070.

[29]G. Keil, Nucl. Instrum. Methods 87, 111 (1970).

[30]B. Barish *et al.*, Caltech Report No. CALT-68-623, 1968 (unpublished).

[31]G. Champion, thesis, Institut des Sciences Nucleaires de Grenoble (ISN), 1979 (unpublished).

[32]The source was made by Amersham, The Radiochemical Centre Ltd., Withe Lion Road, Buckinghamshire England.

[33]H. Kwon, thesis, California Institute of Technology, 1980 (unpublished).

[34]Caltech-ILL-ISN-Munich Collaboration, F. Boehm *et al.*, Phys. Lett. 97B, 310 (1980).

[35]Caltech-Munich-SIN Collaboration, Progress Report, Caltech, 1981 (unpublished).

[36]ISN-Grenoble-LAPP-Annecy Collaboration, Annual Report, ISN, 1980 (unpublished).